

## Some Numerical Experiments on the Withdrawal of Magma From Crustal Reservoirs

FRANK J. SPERA

*Department of Geological and Geophysical Sciences, Princeton University*

Compositional heterogeneity in the form of continuous or discontinuous chemical and thermal gradients in lava and/or pyroclastic flows is very common. An understanding of the dynamics of magma withdrawal is essential to palinspastic reconstruction of intensive variable gradients in magma reservoirs. Important parameters governing the extent of subterranean magma mixing triggered by an eruption include the vertical structure of density and viscosity within the chamber, the discharge, the size and shape of the chamber, and whether eruption takes place along a sublinear fissure, a ring fracture, or a central vent. A numerical model has been set up to study isoviscous magma withdrawal from a central vent conduit as a function of the Reynolds number, the reservoir to conduit width ratio, reservoir aspect ratio (width/depth), and differing kinematic boundary conditions. Both open (magma recharge) and closed (caldera collapse) system behavior are considered. Finite difference solutions to the vorticity transport and Poisson equations enable determination of vorticity, stream function, and velocity fields as a function of time. The most petrologically significant output is the stream function (particle trajectories) and evacuation isochron diagrams. An evacuation isochron represents the locus of points within the chamber such that magma parcels along a given isochron arrive at the bottom of the volcanic conduit concurrently. Open systems evolve toward a time invariant state (fully developed flow). Spin-up times depend on chamber aspect ratio ( $B_r/D_r$ ), reservoir/conduit width ratio ( $B_r/B_c$ ), and Reynolds number ( $Re$ ).  $B_r$ ,  $D_r$ , and  $B_c$  represent chamber half-width, depth, and conduit half-width, respectively. Spin-up times are relatively small (1/10 to 1/5) fractions of typical eruption durations. The shape and orientation of evacuation isochrons (EI) depend on  $Re$  (increasing  $Re$  decreases withdrawal depth) and geometric factors (increasing  $B_r/B_c$  at constant  $Re$  and  $B_r/D_r$ , or decreasing  $B_r/D_r$  at constant  $B_r/B_c$  and  $Re$  increases withdrawal depth). A significant amount of roofward magma can remain untapped in a chamber even for long duration eruptions. Systems driven by caldera collapse also involve juxtaposition of roofward and deep-seated magma during the course of an eruption. Relative to the magma recharge (open system) situation, EI's are laterally elongated. The extent of vertical mixing is thus smaller although still significant in this case. Maximum withdrawal depths vary monotonically in both cases. There is excellent qualitative agreement between predictions based on the numerical experiments and Fe-Ti oxide temperatures for a thermally zoned ash flow deposit south of Mono Lake in eastern California (Bishop Tuff).

### INTRODUCTION

It is a widely held view that the products of many volcanic eruptions represent the rapid and partial evacuation of large subjacent magma reservoirs situated within the crust. In many cases, eruptive products exhibit continuous or discontinuous changes in geochemistry, mineralogy, crystallinity, temperature, and inferred volatile content during the course of a single eruption. These variations may be mapped by densely spaced sampling of well-exposed and continuous vertical sections. For large-volume ( $V > 10^2 \text{ km}^3$ , dense rock equivalent (DRE)) silicic ash flow deposits, careful studies usually reveal a systematic increase in the concentration of mafic components, temperature, crystal content, and magma density and a corresponding decrease in  $\text{H}_2\text{O}$ ,  $\text{SiO}_2$ , and other components stratigraphically upward [Smith, 1960, 1979; Smith and Bailey, 1966; Lipman, 1967; Hildreth, 1979, 1981]. Small- to intermediate-volume silicic ash flow deposits often show similar intradeposit patterns, sometimes with the additional feature of discontinuous changes in magma bulk composition (a compositional gap) at some specific stratigraphic height. Classic examples include the eruption of Mount Mazama ( $V \sim 40 \text{ km}^3$  DRE) [Williams, 1942; McBirney, 1968; Ritchey, 1980; Bacon, 1983], the P1 composite alkali rhyolite to alkali basalt ash flow ( $V \sim 20 \text{ km}^3$  DRE) on Gran Canaria, Canary Islands [Schmincke, 1969, 1972; Crisp, 1983, 1984], the 1912

eruption at Novarupta ( $V \sim 15 \text{ km}^3$  DRE) [Curtis, 1968; Hildreth, 1983], and the 1707 eruption of Mount Fujii ( $V \sim 1 \text{ km}^3$  DRE) [Tsuya, 1955]. Although much less common, eruptions from intermediate to basaltic centers may also exhibit monotonic variations in geochemistry, mineralogy, or phenocryst abundance during the course of a single eruptive cycle. The 1971 eruption of Volcano de Teneguia on the island of La Palma (Canary Islands, Spain) is a good example of a zoned basaltic eruption [Santin et al., 1974]. The late Quaternary Laacher See phonolitic tephra deposit (Eifel, W. Germany), described by Worner and Schmincke [1984], is a well-documented example of mineralogical and chemical zonation in an intermediate-composition system.

The simplest way to interpret the ubiquitous occurrence of compositional and thermal zonation and multiple pumice populations in volcanic deposits from single or closely related eruptions is to postulate the existence of a vertically zoned magma chamber. The realization that volcanological and geochemical studies can be used to reconstruct the pattern of compositional and thermal zonation within a magma chamber is, perhaps, one of the major advances in petrology within the past two decades. This idea has generated interest to students of magmatic transport phenomena, as an understanding of how and at what rate compositional and thermal gradients develop in a chamber is inextricably bound to the larger question of the dynamics of multicomponent-multiphase convection within a rheologically complex viscous fluid. Clearly, solution of this transport problem promises rich rewards that may be important within the larger context of planetary volcanism and crustal evolution.

Copyright 1984 by the American Geophysical Union.

Paper number 4B0514.  
0148-0227/84/004B-0514\$05.00

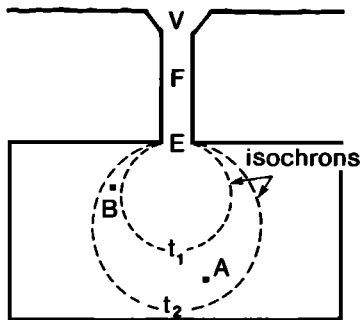


Fig. 1. Schematic portrayal of magma evacuation from a large chamber into a narrow central vent conduit. Times after initiation of the eruption ( $t = 0$ ) are marked on two of an infinite number of evacuation isochrons. In the time interval  $t_2 - t_1$ , magma initially lying between the two isochrons will simultaneously arrive at the bottom entrance of the volcanic conduit (point E). At position F the volume fraction of the vapor in the magma is sufficiently large that the flow is in the compressible (high speed) regime where Mach numbers exceed 0.4 approximately. Due to the high-speed turbulent nature of flow in the pipe, local mixing can be very efficient. Magma parcels located at, say, points A and B will be intimately mixed before they reach the vent (point V).

However, before field and laboratory data can unambiguously be utilized in the reconstruction of preeruptive gradients within a chamber, one must understand and allow for complicated mixing effects that may occur during the eruptive process. Most simply, one may consider mixing to occur in either the subaerial or subterranean realm. Subaerial mixing of a pyroclastic flow could occur either within the vertical eruption column or later during lateral transport immediately preceding emplacement. Although subaerial mixing undoubtedly occurs during a pyroclastic eruption, it is important to note that the time interval a magma parcel spends in the subaerial realm before cessation of movement is usually very short (typically  $10^2$  s) compared with the duration of an eruptive episode (typically  $10^4$ – $10^5$  s). Consequently, despite the turbulent nature of column collapse and lateral transport, the extent of vertical mixing during the subaerial phase remains restricted. If this was not the case, vertical compositional zonation within ash flow deposits would be rare. The common occurrence of vertical compositional zonation indicates that the vertical scale of subaerial mixing is significantly less than the thickness of the deposit.

Subterranean mixing is defined here as the mixing that occurs due to the juxtaposition of magma parcels initially at different depths within the chamber. Mixing occurs in response to magma withdrawal and upwelling through a conduit of much narrower dimension than the larger subjacent reservoir. The most petrologically significant aspect of this process is that magma from many different depths will arrive concurrently at the entrance of the magma conduit (point E, Figure 1) and may therefore become mixed before reaching the vent (point V, Figure 1). The scale of mixing, that is, whether intimate blending of magma or formation of compositionally banded pumice occurs, depends mainly on the viscosity ratio of the two magmas. Even if no subaerial mixing occurs, the stratigraphy of a deposit will not represent the simple inverse zonation within the preeruptive chamber. In order to reconstruct the pattern of preeruptive zonation within a chamber, the magmadynamic withdrawal process should be explicitly accounted for.

It is the purpose of this note to qualitatively discuss the

important parameters governing the relationship between an erupted magma parcel and its sites of origin within a reservoir and to develop a numerical algorithm applicable to the withdrawal of magma from a large reservoir through a central vent conduit. The numerical simulations reported on herein are based on solution of the conservation equations applicable to eruption of incompressible, constant viscosity magma from a large reservoir. The present study is a logical first step in understanding the fluid dynamics of magma withdrawal relevant to complex natural systems.

The method of solution utilized for the numerical simulations allows the calculation of the transient history of the evacuation process at arbitrary Reynolds number within the laminar regime. This is preferable to obtaining only the steady state solution for several reasons. First, the spin-up time for evacuation from a voluminous chamber may be a significant fraction of the duration of the entire eruption. Even for a fixed discharge eruption, the velocity field within the reservoir is time dependent, and so the mixing history will also vary temporally. Second, for the important case where caldera collapse occurs during an eruption, steady flow within the chamber can never really be achieved because of the motion of the sinking caldera roof. Finally, because of the wide range of discharges and transport properties characterizing volcanic eruptions, no single Reynolds number is necessarily applicable in all cases. Calculations have been carried out therefore for a range of Reynolds numbers between the creeping flow ( $Re \rightarrow 0$ ) and subinertial ( $Re \sim 10^3$ ) regimes.

The most important petrological output of the numerical model is the generation of evacuation isochrons for a specific set of geometric, transport, and boundary conditions. These isochrons represent the locus of points in two-dimensional space such that magma parcels along a given isochron arrive at the entrance of the volcanic conduit concurrently. In terms of reconstructing intensive thermodynamic fields in a chamber by surface observation alone, the evacuation isochron diagram is clearly of great significance.

#### MAGMA WITHDRAWAL: QUALITATIVE ASPECTS

A large number of factors govern the relationship between an erupted magma sample and its site of origin within the chamber. For the purposes of discussion, these factors are grouped into the following categories: chamber-conduit geometry, magma transport properties, and dynamic regimes.

#### Geometric Factors

Important geometric factors include the size and shape of the magma reservoir, the relative dimensions of the reservoir and conduit system, and the style of eruption (e.g., ring fracture, fissure, or central vent eruption). In general, there are poor constraints on the sizes and shapes of magma chambers, although in certain specific instances, inferences have been drawn [e.g., Ryan *et al.*, 1983]. Chambers from which voluminous ash flow sheets originate probably have cross-sectional areas on the order of caldera collapse areas and may have relatively flat roofs [Smith, 1979; Spera and Crisp, 1981]. Smaller volume chambers from which less voluminous ash flows are erupted may have conical or pitched roofs [McBirney, 1980]. Based on observed sizes and shapes of large mesozonal to catazonal plutons, it has been suggested that during catastrophic ash flow eruptions, less than about 10% of the volume of the chamber is evacuated [Smith and Shaw, 1973, 1975]. Because of uncertainties regarding chamber shape, a simple flat-topped rectangular shape has been assumed here.

Although the numerical model could easily incorporate other shapes, there is no compelling reason to do so at this time.

The conduit width and the conduit/reservoir width ratio will also influence the style of magma drawdown. For the simple case of inviscid slow motion in a two-layer stratified fluid of infinite lateral extent, Rouse [1956] found a dependence of the critical discharge on the diameter of the conduit as well as the thickness of the low-density fluid layer (see Figure 2). In this case, because the effects of viscosity are ignored and the geometry is very simple, the minimum discharge  $Q$  such that the lower layer will be tapped may be approximately determined. As given by Turner [1973], the condition for lower layer tapping is

$$Q_{\text{crit}} \geq 6.4 \left( \frac{B_c}{g'} \right)^{1/2} h^2 \quad (1)$$

where  $g' \equiv g(\rho_1 - \rho_2)/\rho_1$  and  $h$ ,  $2B_c$ , and  $Q$  represent the thickness of the upper layer, the pipe diameter, and the discharge, respectively. From (1) it is noted that there is a weak dependence of the critical discharge on the conduit width. For example, with  $2B_c = 10$  m, the minimum discharge to ensure tapping of the denser lower layer is  $6 \times 10^4$  m<sup>3</sup>/s; with  $B_c = 100$  m,  $Q$  assumes the value  $1.8 \times 10^5$  m<sup>3</sup>/s. In both cases the values of  $h$ ,  $\rho_1$ ,  $\rho_2$ , and  $g$  are 500 m, 2700 kg/m<sup>3</sup>, 2600 kg/m<sup>3</sup>, and 9.8 m/s<sup>2</sup>, respectively. Note that these discharges are within the range appropriate to pyroclastic eruptions [e.g., see Settle, 1978, Table 1; Wilson et al., 1978, Table 3; Sparks et al., 1978; Wilson, 1976].

A final important geometric factor involves the conduit type. Whether an eruption takes place from a curvilinear ring fracture (or portion of one), a linear fissure (e.g., Hawaiian type rift zone), or a central vent conduit will affect the style of magma withdrawal because of differing kinematic boundary conditions. In this context it is important to note that conduit locations can change even during the course of a single eruption. Bacon [1983], for instance, has shown how the climactic eruption of Mount Mazama 6800 years B.P. began as a central vent eruption ( $V \sim 30$  km<sup>3</sup> DRE) and then changed to a ring fracture phase ( $V \sim 15$  km<sup>3</sup> DRE) that was associated with caldera collapse. In this study, attention will be focused on central vent type eruptions. The Taupo ignimbrite recently described in detail by Walker [1980] and Walker and Wilson [1983] is a good example of a silicic ash flow deposit erupted from a central vent.

#### Transport Properties

Intuitively, one expects that both magma density and viscosity and their variation within the chamber (i.e., continuous variation or discrete layers) will play a role in the details of the withdrawal process. As noted from (1), in a density layered system, the greater the density contrast, the larger the imposed discharge must be to ensure tapping of the lower layer. In a compositionally zoned chamber, high-viscosity, low-density magma will commonly overlie less viscous but denser material. Although no detailed analysis has been carried out, it seems sensible that for a layered system with a given density contrast, as the magnitudes of the viscosities become more disparate, there would be greater tendency for tapping of the lower layer. This would especially be true in the case of a chamber of wide lateral extent. For the small chamber the supply of low-density roofward magma would more quickly become depleted. It might be expected therefore that small-volume systems would tend to tap deeper melts more readily. As noted earlier, this seems consistent with volcanological ob-

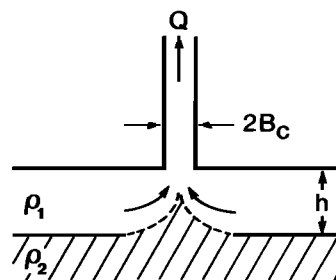


Fig. 2. Geometry of two-layer withdrawal problem, modified from Turner [1973]. For this simplified (inviscid) analysis, a minimum discharge rate  $Q$  must be specified in order that the deeper layer be drawn up into the conduit. The greater the conduit width, the greater the discharge needed for tapping of the lower layer. See text for discussion.

servations. Numerical simulations reported here support this view (Figure 8).

#### Dynamic Regimes

As shown in a later section, for a fixed reservoir-conduit geometry, the only important dynamic variable in the constant viscosity withdrawal problem is the Reynolds number. The Reynolds number ( $Re$ ) is defined for the central vent case according to

$$Re = 3\rho Q/8B_c\eta \quad (2)$$

where  $\rho$ ,  $\eta$ ,  $B_c$ , and  $Q$  represent the magma density, viscosity, conduit radius, and volumetric discharge, respectively. The parameters  $Q$ ,  $\eta$ , and  $B_c$  can each vary quite widely in nature. Measured or inferred discharge rates for basaltic eruptions commonly vary from 10 to  $10^4$  m<sup>3</sup>/s [Delaney and Pollard, 1982; Wadge, 1981, 1982], whereas for silicic caldera-forming eruptions,  $Q$  typically lies in the range  $10^3$ – $10^6$  m<sup>3</sup>/s. Basaltic magma viscosities may be as low as 1 Pa s at liquidus temperatures; high-silica rhyolitic magmas have viscosities as high as  $10^5$  Pa s. Finally, conduit widths vary in diameter in the approximate range 1– $10^2$  m [Erken and Byers, 1976; Shaw and Swanson, 1970] with wide conduits being associated in general with more silicic compositions. Based on this range of parameters, it is noted that  $Re$  may vary by several orders of magnitude, from creeping flow ( $Re \rightarrow 0$ ) to values on the order of  $10^3$ . Of significance here is that for a fixed time interval after initiation of an eruption, the maximum depth of withdrawal varies inversely with  $Re$ . This phenomenon is quantitatively explored in a later section.

#### PREVIOUS WORK

The flow of viscous fluid from a wide channel or reservoir through an abrupt contraction into a narrower pipe is a classical fluid dynamic problem that has attracted much attention since the first recorded observations of eddy formation by Leonardo da Vinci [Rouse and Ince, 1963]. Because of severe mathematical difficulties associated with the nonlinear character of the conservation equations, no closed form analytical solutions have been obtained. Within the last two decades, however, powerful numerical methods have been devised and applied to the unsteady flow of incompressible fluids. The numerical codes developed by Fromm [1964, 1965] and Simuni [1964] are among the earliest and most general ones proposed, although neither of these workers systematically addressed the sudden contraction problem in terms of variations

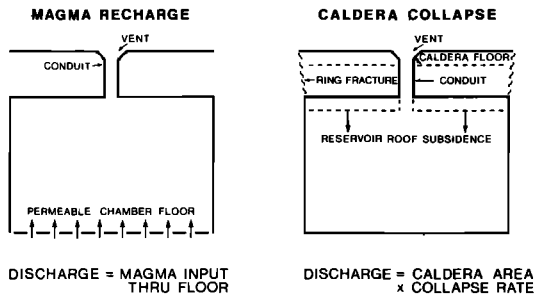


Fig. 3. Two models consistent with magma effusion at discharge  $Q$ . In the magma recharge case, the floor of the chamber is permeable with respect to basic magma injection. In caldera-collapse case, the floor is impermeable; efflux is balanced by chamber roof collapse (caldera subsidence).

in  $Re$ , geometry, and particle trajectories relevant to magma evacuation. Kawaguti [1965] studied steady viscous flow in a channel with a forward (sudden contraction) or backward (sudden expansion) facing step up to  $Re \sim 64$  but at a fixed width ratio of 2. Similarly, Giaquinta and Hung [1968] studied steady flows of incompressible, non-Newtonian fluids in a two-dimensional conduit expansion for Reynolds numbers between 0 and 16 and a fixed channel diameter ratio of 2. Their work was mainly concerned with a systematic study of eddy characteristics and pressure losses as a function of power law index. They found that the departure from Newtonian behavior decreased as  $Re$  increased and that this decrease was much greater for dilatant than pseudoplastic fluids. Other workers, including Dennis and Smith [1980], Holstein and Paddon [1982], and Peyret and Taylor [1983], have focused attention on the flow in the neighborhood of a reentrant corner at low  $Re$  number, again for an entry/exit width ratio of 2.

In a volcanological context the only previous work done on this problem is the study by Blake [1981]. He applied the approximate analytic solution of Weissberg [1962] to obtain the velocity field within a large flat-topped reservoir from which a constant viscosity fluid moves radially into an exit conduit. The solution is for steady state flow in the creeping flow ( $Re \rightarrow 0$ ) regime and is based on an approximate variational technique. An important contribution of his work was the determination of what are called here evacuation isochrons. These clearly show that in the region below the orifice and extending laterally, juxtaposition of magma initially at distinct depths occurs during withdrawal.

#### MODEL

##### General Features and Assumptions

In light of inherent limitations in the aforementioned studies, this work was initiated to study the topology of evacuation isochrons as a function of  $Re$ , the reservoir/conduit width ratio, unsteady effects, and boundary conditions. Boundary conditions were chosen to simulate either caldera collapse or open-system behavior (Figure 3). In the caldera collapse version, magma efflux through the central vent conduit is balanced by collapse (downward movement) of the chamber roof. The open-system model is characterized by magma recharge through the "floor" of the chamber sufficient to offset the constant discharge through the exit conduit. The caldera collapse model is probably most relevant to large-volume intermediate to silicic composition pyroclastic eruptions, which in fact, are commonly associated with caldera collapse. The recharge model, on the other hand, may be more

relevant to eruptions from basaltic chambers, where chamber replenishment occurs due to deeper magma upwelling. In both cases studied,  $Q$  is constant.

The simulations have been carried out assuming two-dimensional flow of a constant viscosity, incompressible Newtonian fluid. The assumption of incompressibility is not as poor as it may first seem. Although volatile-rich magma may achieve transonic velocities in the vicinity of the vent [Wilson *et al.*, 1980; Housley, 1978; Kieffer, 1982; Spera, 1982, 1983], the Mach number  $M$  of magma flowing into the base of the conduit (point E, Figure 1) remains within the subsonic incompressible flow regime (i.e.,  $M < 0.35$  [Shapiro, 1953; Shames, 1982]). In order to show that this must generally be the case, consider the magma velocity at the entrance of a conduit in order to explain the most intense of eruptions. Wilson *et al.* [1978] suggest an upper limit of  $10^6$  m<sup>3</sup>/s for magma discharge (DRE) based on an analysis of volcanic eruption column heights. Most observed eruptions discharge at considerably lower rates in the range  $10-10^5$  m<sup>3</sup>/s (references previously cited). Adopting a typical vent diameter of 100 m [Erken and Byers, 1976; Cook, 1968; Korrington and Noble, 1970] and the upper limit of discharge ( $10^6$  m<sup>3</sup>/s), the average magma velocity in the conduit is  $V = Q/A \sim 150$  m/s. Now consider the isentropic sound speed of multiphase water-rich (melt + 8 wt % H<sub>2</sub>O) rhyolite magma at 850°C and  $P_t = 100$  MPa. Under these conditions the concentration of H<sub>2</sub>O dissolved in the melt ( $\rho = 2300$  kg/m<sup>3</sup>) is about 4.3 wt % [Shaw, 1974]. Partitioning of H<sub>2</sub>O between the vapor and melt phases indicates a volume fraction of vapor phase of about 25%, well below the fragmentation limit ( $\sim 70\%$ ). The square of the sound speed of this mixture is approximately

$$C^2 = \frac{\rho_v}{\rho_m} \frac{C_v^2}{\alpha(1-\alpha)} \quad (3)$$

where  $\rho_v$ ,  $\rho_m$ ,  $\alpha$ ,  $C_v$ , and  $C$  represent the density of vapor and melt, volume fraction vapor phase, isentropic sound speed in the vapor phase, and magma (mixture) sonic velocity, respectively [Wallis, 1969; Helgeson *et al.*, 1978; Carmichael *et al.*, 1977]. In this extreme example the magma sound speed is about 600 m/s. At the bottom entrance of the conduit therefore,  $M = V/C \sim 0.25$ , which is still within the range cited for subsonic incompressible flow.

The most severely constraining assumption of the present model is that of constant viscosity within the chamber. The results presented here are therefore most directly applicable to chambers of either constant composition (e.g., basaltic chambers) or to systems where the roofward enrichment of

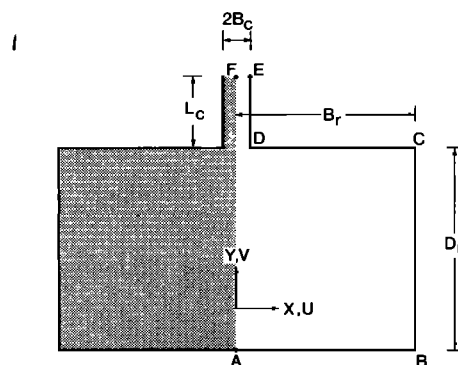


Fig. 4. Configuration of reservoir-conduit system used for computations.

H<sub>2</sub>O offsets the roofward enrichment in SiO<sub>2</sub> to give an approximately constant viscosity. In a layered system (e.g., rhyolite above basalt) the viscosity contrast may be quite large ( $\eta_1/\eta_2 \sim 10^3$ ), and clearly, a constant viscosity model is inappropriate. Although quantitative questions regarding the extent of vertical mixing in such a strongly stratified system cannot be addressed by the model presented here, that mixing does occur is clearly indicated by the propensity of mixed magmas in pyroclastic systems [Smith, 1979].

#### Model Geometry

In Figure 4 the configuration of the reservoir-conduit system is shown. Calculations were carried out for a two-dimensional rectangular coordinate system. As is evident from Figure 4, the  $y$  axis is a line of symmetry (mirror plane), and consequently, calculations need be carried out only within one side of the spatial domain (in region ABCDEF). This affords considerable time and cost savings, as the computational domain is effectively cut in half.

There are two independently variable length ratios relevant to magma withdrawal from a finite volume reservoir. These include the conduit/reservoir width ratio ( $B_c/B_r$ ) and the reservoir width/depth ratio ( $B_r/D_r$ ). In all the simulations reported here, the length of the volcanic conduit  $L_c$  was long enough to ensure fully developed vertical flow within the pipe; lengthening  $L_c$  beyond this limit had no effect on computed solutions. Conclusions drawn in this study are based on numerical experiments for which  $B_c/B_r$  varied from 1/5 to 1/40 and  $B_r/D_r$  varied from 1/2 to 2.

#### Differential Equations and Nondimensionalization

The Navier-Stokes equations applicable to unsteady flow of an incompressible Newtonian fluid of viscosity  $\eta$  and density  $\rho$  in two dimensions are

$$\rho \left( \frac{\partial u}{\partial t} + u \frac{\partial u}{\partial x} + v \frac{\partial u}{\partial y} \right) = -\frac{\partial p}{\partial x} + \eta \left( \frac{\partial^2 u}{\partial x^2} + \frac{\partial^2 u}{\partial y^2} \right) \quad (4)$$

and

$$\rho \left( \frac{\partial v}{\partial t} + u \frac{\partial v}{\partial x} + v \frac{\partial v}{\partial y} \right) = -\frac{\partial p}{\partial y} + \eta \left( \frac{\partial^2 v}{\partial y^2} + \frac{\partial^2 v}{\partial x^2} \right) - \rho g \quad (5)$$

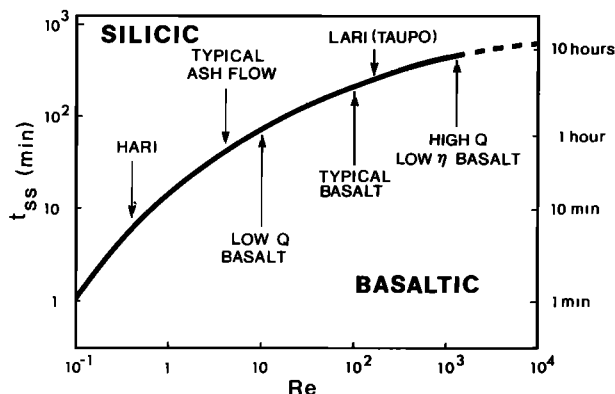


Fig. 5a. Time to attain fully developed (steady state) flow in a chamber as a function of  $Re$ . Reynolds number is related to discharge, conduit size, magma density, and viscosity by (2). Dimensional times are given for the case  $D_r/B_r \sim 1/2$ ,  $B_r/B_c \sim 20$ , and  $B_c = 100$  m. The Reynolds numbers for silicic and mafic composition systems are shown. LARI refers to low aspect ratio ignimbrite and HARI to high aspect ratio ignimbrite of Walker [1981]. LARI is characterized by a relatively low  $Q$  ( $\sim 10^4$  m<sup>3</sup>/s), and HARI by high discharge ( $\sim 10^6$  m<sup>3</sup>/s).

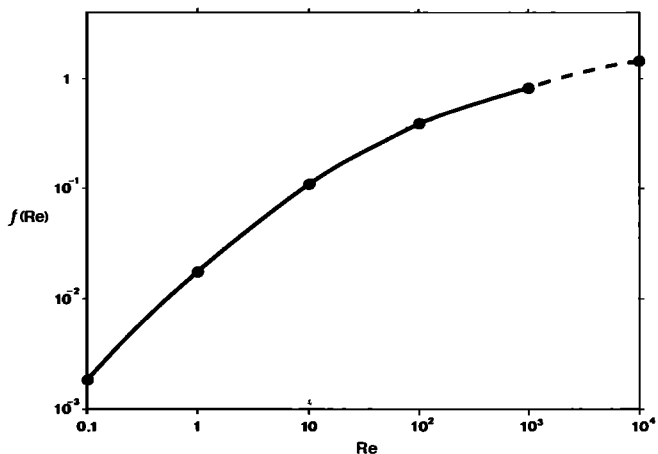


Fig. 5b. The function  $f(Re)$  of (26) as a function of Reynolds number. Note that  $f(Re)$  versus  $Re$  gives a slope near unity at low  $Re$  as deduced in Appendix B. As discussed in text,  $f(Re)$  is independent of reservoir-conduit relative dimensions and consequently may be used in conjunction with (26) to calculate times necessary for attainment of fully developed flow within any size chamber.

Conservation of mass requires that

$$\frac{\partial u}{\partial x} + \frac{\partial v}{\partial y} = 0 \quad (6)$$

It is convenient to define a stream function  $\psi$  according to

$$u \equiv \frac{\partial \psi}{\partial y} \quad v \equiv -\frac{\partial \psi}{\partial x} \quad (7)$$

and  $\omega$ , the vorticity, as

$$\omega = \frac{\partial v}{\partial x} - \frac{\partial u}{\partial y} \quad (8)$$

Since the definition of the stream function automatically satisfies the continuity expression, it is no longer necessary to consider (6). When (7) and (8) are combined, an elliptic Poisson equation of the form

$$\frac{\partial^2 \psi}{\partial x^2} + \frac{\partial^2 \psi}{\partial y^2} = -\omega \quad (9)$$

results. Equation (9) is essentially a statement of mass conservation in terms of the stream function and vorticity.

The vorticity transport equation may be derived by differentiation of (4) with respect to  $y$  and (5) with respect to  $x$  and then subtracting the resulting expressions. Introducing the definition of the vorticity (8), one finally arrives at

$$\frac{\partial \omega}{\partial t} + u \frac{\partial \omega}{\partial x} + v \frac{\partial \omega}{\partial y} = \nu \left( \frac{\partial^2 \omega}{\partial y^2} + \frac{\partial^2 \omega}{\partial x^2} \right) \quad (10)$$

which is the desired vorticity transport equation. The kinematic viscosity  $\nu$  is defined as  $\eta/\rho$ . Note that the parabolic vorticity transport equation consists of an unsteady term ( $\partial\omega/\partial t$ ), the inertial terms  $u(\partial\omega/\partial x)$  and  $v(\partial\omega/\partial y)$  and the viscous diffusion term  $\nu\nabla^2\omega$ .

Equations (7)–(10) constitute four equations in the unknowns  $u$ ,  $v$ ,  $\psi$ , and  $\omega$  and represent the system of equations that must be solved along with boundary conditions in order to simulate magma evacuation from a crustal reservoir. Boundary conditions used to generate solutions in this work are given in the next section.

It is convenient to nondimensionalize (7)–(10) to facilitate

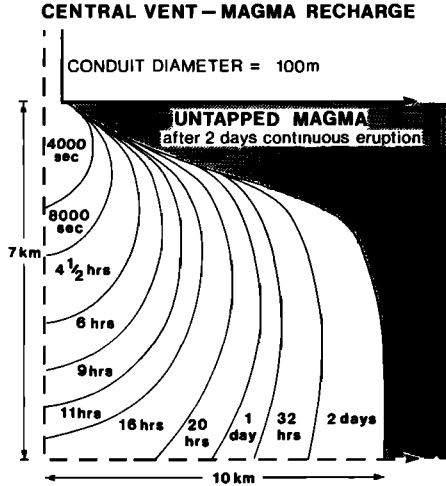


Fig. 6a. Evacuation diagram for  $Re = 10^2$ ,  $B_r/B_c \sim 20$ , and  $B_r/D_r \sim 2$ .

the numerical analysis. This is accomplished by defining a velocity scale according to

$$V = \frac{3Q}{8B_c^2} \quad (11)$$

where  $Q$  is the discharge (a constant during a simulation). Equation (11) defines the maximum velocity along the centerline of the conduit modeled here as an equant duct. The maximum vertical velocity occurs at the top of conduit. Adopting the half-width of the conduit  $B_c$  as the reference length, the following nondimensional variables may be defined:

$$\begin{aligned} \bar{u} &= \frac{u}{V} & \bar{v} &= \frac{v}{V} & \bar{t} &= \frac{Vt}{B_c} \\ \bar{x} &= \frac{x}{B_c} & \bar{y} &= \frac{y}{B_c} & \bar{\omega} &= \frac{B_c \omega}{V} \\ \bar{\psi} &= \frac{\psi}{VB_c} & \bar{R} &= \frac{B_c}{B_r} \end{aligned} \quad (12)$$

where all barred quantities are nondimensional. Introducing (12) into (7) through (10), the relevant equations take on the following form.

Vorticity transport

$$\frac{\partial \bar{\omega}}{\partial \bar{t}} + \bar{u} \frac{\partial \bar{\omega}}{\partial \bar{x}} + \bar{v} \frac{\partial \bar{\omega}}{\partial \bar{y}} = \frac{1}{Re} \left[ \frac{\partial^2 \bar{\omega}}{\partial \bar{x}^2} + \frac{\partial^2 \bar{\omega}}{\partial \bar{y}^2} \right] \quad (13)$$

Poisson equation

$$\frac{\partial^2 \bar{\psi}}{\partial \bar{x}^2} + \frac{\partial^2 \bar{\psi}}{\partial \bar{y}^2} = -\bar{\omega} \quad (14)$$

Vorticity

$$\bar{\omega} = \frac{\partial \bar{v}}{\partial \bar{x}} - \frac{\partial \bar{u}}{\partial \bar{y}} \quad (15)$$

Stream function

$$\bar{u} = \frac{\partial \bar{\psi}}{\partial \bar{y}} \quad \bar{v} = -\frac{\partial \bar{\psi}}{\partial \bar{x}} \quad (16)$$

where the Reynolds number, defined according to

$$Re = \frac{\rho V B_c}{\eta} \quad (17)$$

is the only parameter of the problem.

In the remainder of this paper, bars are dropped from all symbols. Unless explicitly stated, all variables discussed are the nondimensional ones as defined in this section.

### Boundary Conditions

Different sets of boundary conditions were used depending on whether the magma recharge (case 1) or caldera collapse (case 2) model was being studied (see Figure 3). In addition, for the magma recharge case, two different velocity profiles were used along the bottom of the chamber (AB on Figure 4): parabolic and uniform velocity. Not surprisingly, the velocity field and hence the shape and position of evacuation isochrons were little affected by the shape of the influx velocity profile. Only for unrealistically large values of  $B_r/D_r$ , (i.e.,  $B_r/D_r > 10$ ) does the influx velocity field significantly influence the stream function and vorticity fields in the interior of the chamber.

Because of symmetry relations previously noted,  $u = \omega = 0$  along AF. Boundary AF also represents a streamline, so that  $\psi = \text{const}$ . For consistency with velocity profiles along FE and AB,  $\psi$  is set equal to zero along AF. The vertical velocity  $v$  along AF is part of the solution and is not set a priori. These conditions along AF are valid for both case 1 and case 2.

Case 1. Along FE the following conditions are set:

$$v = 1 - x^2 \quad u = 0 \quad (18)$$

$$\omega = -2x \quad \psi = \frac{1}{3}x(x^2 - 3)$$

That is, parabolic fully developed flow is assumed in the far upstream portion of the conduit. The vorticity and stream function follow from their defining equations ((7) and (8)). Along boundaries ED, DC, and CB,  $u = v = 0$  and  $\psi = -2/3$ . The stream function value along these boundaries follows from (18) and the fact that the boundary EDCB represents a stream line. Finally, along AB for the parabolic profile,

$$\begin{aligned} v &= \frac{1}{R} \left[ 1 - \left( \frac{x}{R} \right)^2 \right] & u &= 0 \\ \psi &= \frac{1}{3} \frac{x}{R} \left[ \left( \frac{x}{R} \right)^2 - 3 \right] \\ \omega &= -\frac{2x}{R^3} \end{aligned} \quad (19)$$

whereas for uniform flow,

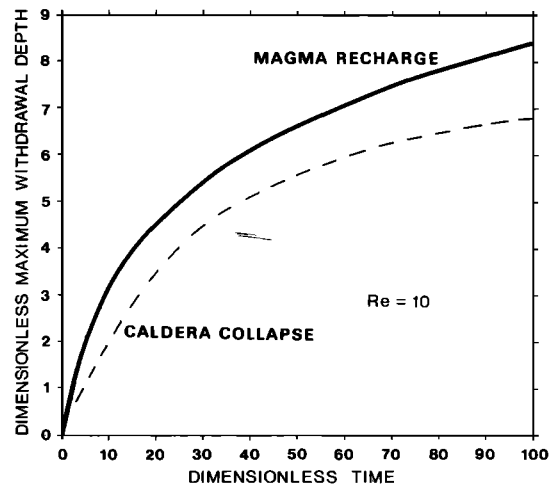


Fig. 6b. Maximum withdrawal depth versus time of eruption for magma recharge and caldera collapse situations.  $Re = 10$ ,  $B_r/B_c = 20$ , and  $B_r/D_r \sim 2.2$  for both cases.

$$\begin{aligned}
 v &= \frac{2}{3}R & u &= 0 \\
 \psi &= -\frac{2}{3}Rx \\
 \omega &= 0
 \end{aligned}
 \tag{20}$$

Case 2. In the caldera collapse model, the removal of magma from the reservoir is balanced by the volume decrement due to roof collapse. The bottom of the chamber is assumed to be impervious in this case (i.e., AB is an impermeable no-slip boundary). Conservation of mass necessitates therefore that

$$\int_0^1 v \, dx = \int_1^{x_m} v_r \, dx
 \tag{21}$$

where  $v$  is the velocity along FE ( $v = 1 - x^2 + v_r x^2$ ) and  $v_r$  is the velocity (assumed constant) of the foundering roof. Assuming a parabolic velocity along FE, (21) implies that  $v_r = (1 - \frac{3}{2}x_m)^{-1}$ , where  $x_m = R^{-1}$  (see (12)), is the reservoir/conduit width ratio. The stream function and vorticity along FE follow immediately upon specification of  $v$  such that

$$\psi = \frac{x^3}{3} (1 - v_r) - x \quad \omega = 2x(v_r - 1)
 \tag{22}$$

Since the flow is fully developed along FE, the horizontal velocity vanishes identically there. Along wall ED the following boundary conditions apply:

$$\begin{aligned}
 u &= 0 & v &= v_r \\
 \psi &= \frac{1}{3}(v_r + 2)
 \end{aligned}
 \tag{23}$$

Similarly, along DC, the no-slip, caldera collapse and stream function conditions are

$$\begin{aligned}
 u &= 0 & v &= v_r \\
 \psi &= \frac{2}{3}(v_r - 1) - v_r x
 \end{aligned}
 \tag{24}$$

The boundaries CB and AB represent a stream line. This, together with the no-slip condition, gives

$$u = v = \psi = 0
 \tag{25}$$

along both (CB and AB) boundaries.

THE ALGORITHM

The common practice of defining a uniform finite difference mesh has been employed here. The indices  $i, j$  refer to the location of grid points corresponding to intersections of mesh

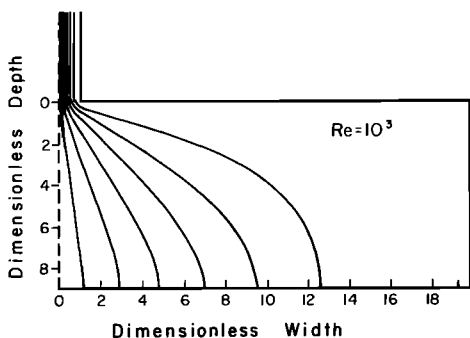


Fig. 7a. Stream function plot for  $Re = 10^3$ ,  $B_r/B_c = 20$ , and  $B_r/D_r = 2.2$  for fully developed flow in the magma recharge case. Vertical depth axis is AF in Figure 4 for which  $\psi = 0$ , and  $-\psi$  varies from 0 to  $2/3$  in equal increments.

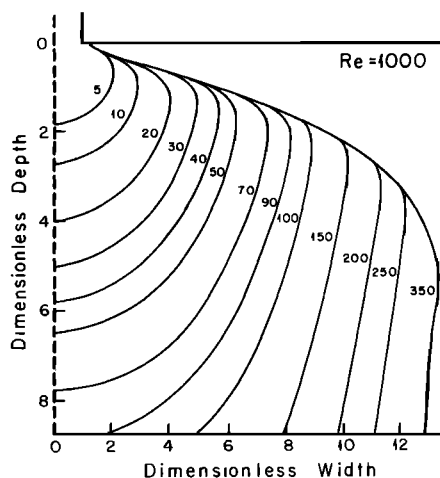


Fig. 7b. Evacuation isochrons (EI) for parameters of Figure 7a. Isochrons are labeled by dimensionless times.

lines parallel to the  $x$  and  $y$  directions, respectively. The solutions to finite difference forms of (13)–(16) are found at a finite number of grid points ( $i, j$ ) in the computational domain. The spacing of the grid points is intimately related to the stability, accuracy, and cost of a simulation. In Appendix A are details of the finite difference methods used for the computation of all fluid dynamic field variables (i.e.,  $\psi, \omega, u,$  and  $v$ ), comments on the accuracy and stability of solutions, and the techniques used to track magma parcels in the Lagrangian mode for evacuation isochron determination. The books by Roache [1972] and Peyret and Taylor [1983] are recommended as general reference works to those desirous of a general introduction to extant methods in computational fluid dynamics.

RESULTS

Introduction

A large number of numerical simulations were performed so that the effects of different boundary conditions, reservoir-conduit dimensions, chamber volumes, and Reynolds numbers

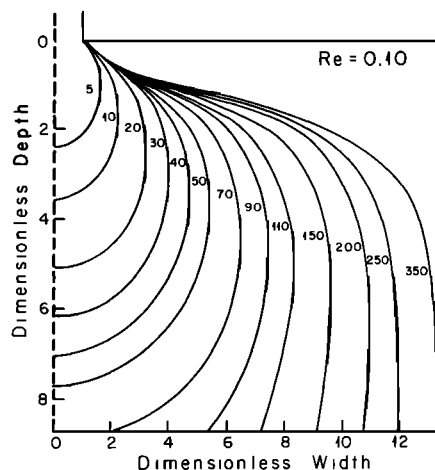


Fig. 7c. EI for  $Re = 0.10$ . Dimensions of reservoir/conduit identical to Figure 7a. Note the vertical elongation of isochrons compared with Figure 7b. Although the shape of isochrons is a function of  $Re$ , the volume of the stagnant zone near the chamber roof is only weakly dependent on  $Re$ . Volume of stagnant zone correlates more directly with chamber size and shape.

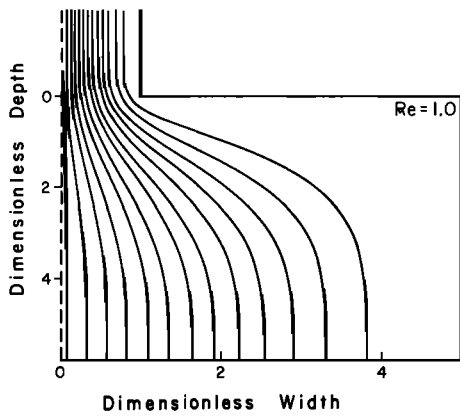


Fig. 8a

Fig. 8. Stream function and EI diagrams illustrating effects of chamber geometry on magma withdrawal.  $Re = 1$  in all cases. Analysis of these and related simulations indicates that increasing  $B_r/B_c$  at constant  $B_r/D_r$  or decreasing  $B_r/D_r$  at constant  $B_r/B_c$  creates a larger volume of roofward untapped magma. (a)  $B_r/B_c = 5$ ,  $B_r/D_r = 1$ ,  $-\psi$  varies from 0 to 2/3 in equal increments. (b)  $B_r/B_c = 5$ ,  $B_r/D_r = 1/2$ , streamlines as in Figure 8a. (c) EI for Figure 8b. (d)  $B_r/B_c = 40$ ,  $B_r/D_r = 2$ . (e) EI for Figure 8d.

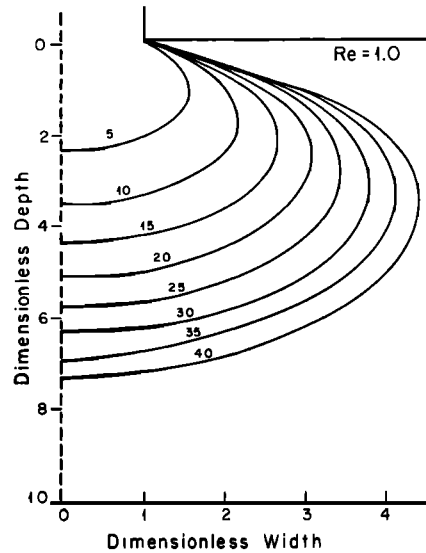


Fig. 8c

except along boundaries AB and EF as indicated by (18), (19), or (20). Field variables ( $\psi$ ,  $\omega$ ,  $u$ , and  $v$ ) subsequently undergo a transient development (spin-up) and finally reach a steady state after some finite time has elapsed. This duration, denoted as  $t_{ss}$ , can be shown from dimensional analysis to depend only on the dimensions of the chamber and the Reynolds number. That is,

$$t_{ss} = \left(\frac{D_r}{B_c}\right) \left(\frac{B_r}{B_c}\right) f(Re) \tag{26}$$

where the function  $f(Re)$  must be determined by numerical experiment. It may be anticipated from a simple analysis (see Appendix B) that  $t_{ss}$  is directly proportional to  $Re$  in the creeping flow regime. The dependence of  $t_{ss}$  on  $Re$  becomes weaker as  $Re$  increases until finally in the turbulent range ( $Re > 2 \times 10^3$ ) the spin-up time becomes independent of  $Re$ . That is,  $t_{ss}$  is a monotonically increasing function of  $Re$  that approaches asymptotic behavior in the turbulent regime. Therefore low  $Re$  eruptions will be associated with shorter spin-up times compared with high  $Re$  eruptions. It is impor-

could be systematically explored. Additionally, transient information could be obtained for cases where a steady state solution exists. Stream function plots (i.e., particle paths) were constructed by smoothing and interpolation of stream function values at nodal points, and evacuation isochrons were determined by tracking of inert markers along streamlines. It will be noted therefore that each simulation generated a large amount of information. In the interests of brevity, only some of the more salient features of the solutions are considered here as they apply to the magma evacuation problem. Most of the results presented in this section are given in terms of dimensionless quantities, as this is the most concise means of information transmission. For the sake of illustration, however, some dimensional results are also cited.

Case 1: Magma Recharge

Spin-up time. The imposed initial condition is that  $u = v = 0$  everywhere within the computational domain

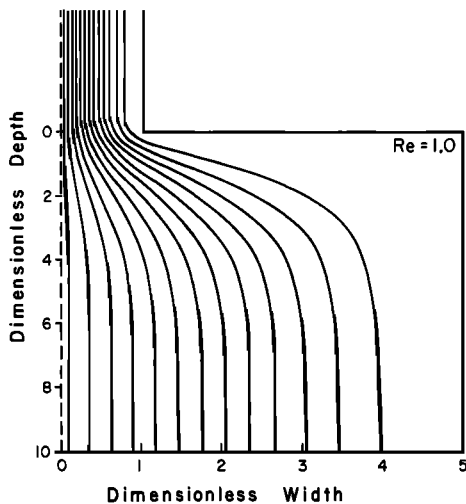


Fig. 8b

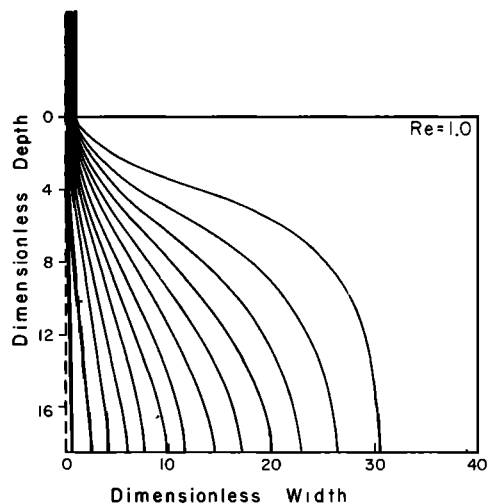


Fig. 8d

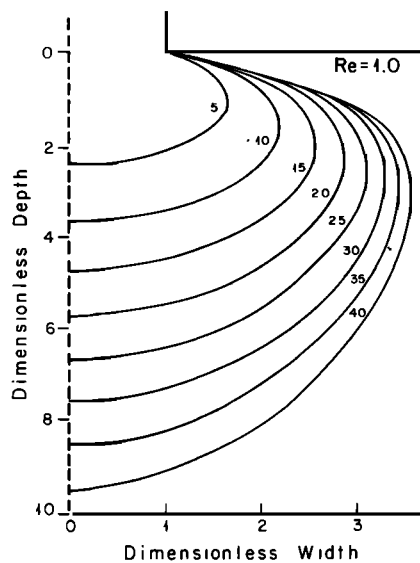


Fig. 8e

tant to note that the time dependence referred to here is unrelated to unsteadiness in magma discharge. Rather it refers to the developing velocity field with the chamber.

Figure 5a gives the results of a series of numerical experiments that corroborate the deductions made above. Note that for small  $Re$ ,  $t_{ss}$  depends linearly on  $Re$ , whereas as  $Re$  increases,  $t_{ss}$  becomes nearly independent of  $Re$ . The results shown in the figure are for the particular values of  $D_r/B_c = 9$  and  $B_r/B_c = 20$ . In Figure 5b the dependence of  $f(Re)$  on  $Re$  is shown; the results in Figure 5b are independent of chamber size. Figure 5b used in conjunction with (26) enables one to determine the spin-up time for any size magma chamber. As a specific example, consider  $t_{ss}$  for an eruption from a chamber 10 km deep with a cross-sectional area of 400 km<sup>2</sup> and conduit diameter of 100 m. As additional parameters assume  $Q = 5 \times 10^4$  m<sup>3</sup>/s and  $\nu = 10$  m<sup>2</sup>/s ( $\eta \sim 2 \times 10^5$  P). Then from (2),  $Re \sim 50$ , and from Figure 5b and from (11), (12), and (26) the spin-up time is approximately 22 hours. The volume of erupted magma at this time would be about 4 km<sup>3</sup> (DRE). Note that the spin-up time represents a significant period of time (nearly a day) relative to a typical eruption duration.

#### Stream Function and Evacuation Isochrons

**Magma withdrawal.** In Figure 6a a dimensional cross section of a large aspect ratio ( $B_r/B_c \sim 20$ ) magma chamber is shown with illustrative evacuation isochrons. Time is measured with respect to the initiation of the eruption ( $t = 0$ ), and the discharge is constant throughout the 2-day eruption. In this example the spin-up time is about 6 hours, at which time magma from a depth of 5 km is mixing with material near the top of the reservoir. Note that as the eruption proceeds, the fraction of "deep" magma increases monotonically. Figure 6b shows the variation of maximum withdrawal depth versus time for both the recharge (open system) and caldera collapse models. As an eruption proceeds, the extent of potential vertical mixing is seen to increase. A significant volume of magma can remain trapped in a "backwater" region near the roof of the chamber during the course of an eruption. The size and shape of this stagnant region depend on the relative dimensions of a chamber and on whether magma recharge or caldera collapse balances the rate of magma withdrawal (cf. Figures 9b and 9c).

**Mixing depth versus  $Re$ .** Figure 7 compares  $\psi$  and isochron plots for fully developed ( $t = t_{ss}$ ) flows with  $B_r/D_r = 2.2$  and  $B_r/B_c = 20$  for  $Re = 0.1$  and  $Re = 10^3$ . A comparison of isochron diagrams (Figures 7b and 7c) shows the effect of  $Re$  on mixing depth. The effect of increasing  $Re$  is to decrease the vertical scale over which mixing occurs. All other factors being equal, a high Reynolds number eruption from a zoned or layered chamber would show less compositional heterogeneity than a low  $Re$  eruption from the same chamber. For example; at a dimensionless  $t = 50$  and for  $B_c = 100$ , the low  $Re$  eruption would mix magma over a depth range of 3.2 km versus only 2.5 km for the high  $Re$  eruption. The stream function field shows that the assumption of radial flow in the reservoir breaks down at large distances from the conduit entrance.

**Effects of chamber size.** Figure 8 compares  $\psi$  and evacuation isochron systematics for chambers of different aspect ratios and widths. All results are for  $Re = 1$  at times corresponding to fully developed flow throughout the chamber. Analysis of these and other numerical experiments (not shown) indicates that both the reservoir/conduit width ratio and reservoir/depth length ratio are quantitatively important parameters with respect to the shape and orientation of evacuation isochrons. Comparison of EI plots shows that for fixed  $Re$  and  $B_r/D_r$ , increasing  $B_r/B_c$  (i.e., making the chamber wider relative to the conduit) makes for a larger volume of roofward stagnant magma that remains untapped even for long duration eruptions. Similarly, for fixed  $B_r/B_c$ , making the chamber deeper (decreasing  $B_r/D_r$ ) also leaves a larger amount of untapped magma in the region directly underlying the roof of the reservoir. A corollary of the stagnation phenomenon is for magma to be drawn from deeper levels and hence for the extent of potential vertical mixing to be maximized relative to cases where a higher fraction of roofward magma is erupted.

#### Case 2: Caldera Collapse

In Figures 9a, 9b, and 9d,  $\psi$  and isochron diagrams are shown for magma evacuation driven by caldera collapse. Steady solutions cannot be found in this case because of the decreasing depth of the reservoir. The vorticity field (not shown) shows considerably more rapid spatial variation due to the perturbing role of the subsiding roof. The stream function diagram (Figure 9a) indicates that the foundering roof acts as a piston and forces magma to move laterally toward the conduit. Within the conduit there is a very thin zone adjacent the subsiding block where magma is dragged down, although this generally cannot be resolved due to coarseness of the grid. This is a consequence of the no-slip boundary condition on  $v$  and represents an additional source of vorticity absent in the recharge problem.

The effect of roof foundering is clear in the evacuation isochron diagram (Figure 9b). Relative to the magma recharge case, the isochrons are laterally elongated. This implies that the extent of vertical mixing will be less than in the recharge case, although clearly, magma juxtaposition remains a prominent feature of the withdrawal process. Field evidence [see Lipman, this issue] suggests that vertical relief due to caldera collapse is commonly in the range  $10^2$ – $10^3$  m, so that roof subsidence is probably a relatively small fraction of the chamber depth. Comparison of Figures 9b and 9c illustrates the difference between the magma recharge and caldera collapse models in terms of evacuation isochrons, all other factors being identical. The important features are that (1) maximum withdrawal depth versus time grows at a much slower rate (Figure 6b) and (2) the volume of the stagnant (untapped)

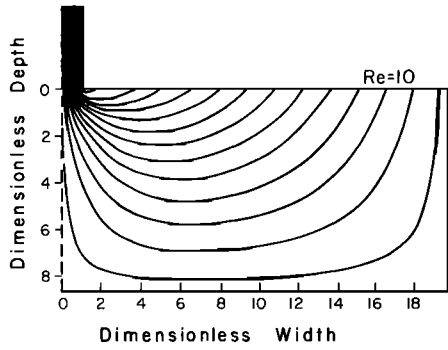


Fig. 9a. Stream function plot for caldera collapse case  $Re = 10$ ,  $B_r/B_c = 20$ , and  $B_r/D_r = 2.2$ . Stream function field for roof collapse is equal to 1% of initial chamber depth ( $D_r$ ), and  $-\psi$  varies from 0 to  $2/3$  in equal increments.

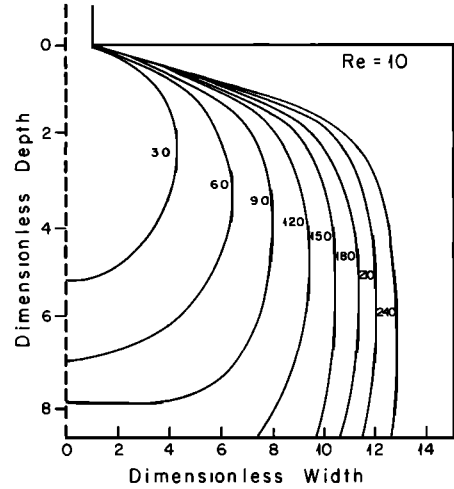


Fig. 9c. EI plot for magma recharge case with some  $Re$  and geometry as in Figures 9a and 9b. Direct comparison of Figures 9c and 9b shows significant differences in the pattern of magma withdrawal, although an appreciable amount of juxtapositional mixing occurs in both cases.

region is much smaller for the caldera collapse case. Figure 9d shows EI for a wider and deeper chamber at  $Re = 100$ . This illustrates again the flattened shape of the isochrons for the caldera collapse situation.

SUMMARY OF PETROLOGICAL IMPLICATIONS

Caution is recommended in applying the results of the numerical simulations to specific volcanic eruptions. Only a small fraction of possible chamber sizes and shapes, vent locations (ring fracture, central vent, fissure), and density-viscosity variations have been studied to date. Modeling of ring fracture eruptions can be accomplished in a straightforward manner by changes in boundary conditions along AF (Figure 4). Preliminary simulations show that the juxtaposition of magma from an even wider depth range occurs for a ring fracture eruption relative to the central vent case. Perhaps the most important limitation in the numerical experiments reported on herein is the assumption of constant density and viscosity within the reservoir.

Despite these limitations, several features of the present model are probably of general qualitative, if not semiquantitative, significance to the dynamics of magma withdrawal and the interpretation of compositional and thermal zonation in ash flow deposits.

1. As an eruption proceeds, the maximum depth of with-

drawal increases monotonically (Figure 6b). An obvious implication of this is that systematic changes in temperature and composition of erupted products will occur during the course of any eruption. In Figure 10, temperature data from *Hildreth* [1977] are presented for the extracaldera facies of the Bishop Tuff, a Quaternary ignimbrite deposit in eastern California. Two features of these data are especially important. First, as the eruption proceeded, the mean temperature of erupted magma increased from 720°C to about 780°C. Second, as the eruption progressed, the temperature span at a given stratigraphic horizon increased from a few degrees for the earliest phase of the eruption to greater than 50°C for the last phase (Mono Basin flow unit). Both features are qualitatively predictable from evacuation isochron diagrams assuming thermal gradients existed within the chamber. It is hoped that further refinements and extensions of the numerical model will allow use of temperature information to differentiate central vent from ring fracture eruptions driven by either caldera collapse or magma recharge.

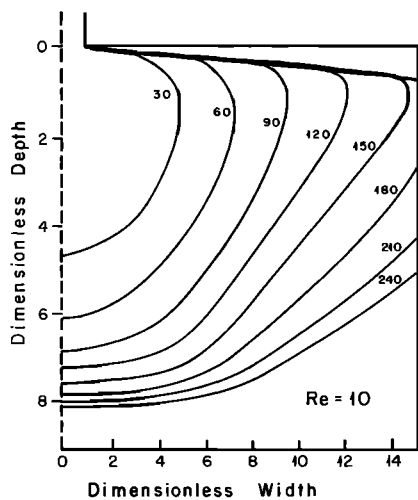


Fig. 9b. EI plot for simulation described in Figure 9a.

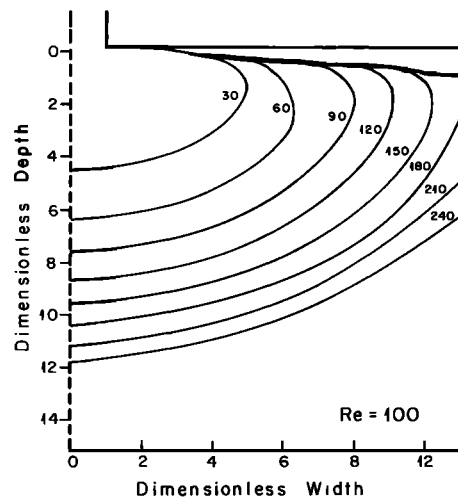


Fig. 9d. IC plot for caldera collapse case with  $Re = 100$ ,  $B_r/B_c = 30$ , and  $B_r/D_r = 1$ .

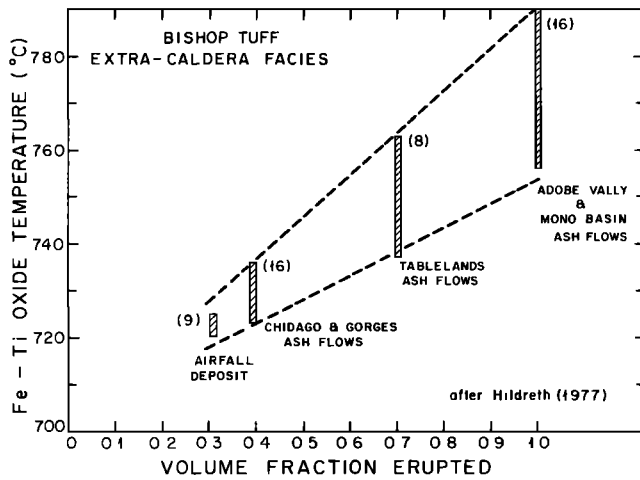


Fig. 10. Fe-Ti oxide temperatures of fresh pumice samples as a function of eruptive fraction for the extracaldera facies of the Bishop Tuff, California. Numbers in parentheses refer to the number of independent temperatures for each phase of the eruption. Data from Hildreth [1977]. The fact that both mean temperatures and standard deviations increase with fraction erupted is consistent with the models presented here.

2. Examination of the evacuation isochron diagrams reveals that a significant portion of magma initially roofward in a chamber but at a lateral distance from the conduit will not be erupted, especially for chambers of large  $B_r/B_c$  and small  $B_r/D_r$ . This effect is most dramatic for the magma recharge situation, although the phenomenon persists in situations characterized by caldera collapse. Note that evacuation isochron envelopes become tangential to a single curve in  $x$ - $y$  space. Magma lying above this curve remains in the chamber despite its proximity to the roof. This implies that estimates of the rate of production of evolved magma, as inferred by ash flow volume-repose time systematics [e.g., Spera and Crisp, 1981], are maximal values, since all of the evolved magma present in a given chamber will not be erupted even when deeper (mafic) magma has been tapped. Furthermore, the stagnation effect is intensified as the ratio of reservoir width/conduit width ( $B_r/B_c$ ) increases. As a consequence, volumetric rates for production of evolved (high  $\text{SiO}_2$ ) magma as inferred from eruptive volume-repose time systematics might be biased toward high values for smaller systems when, in fact, in situ rates are comparable.

3. In Figures 9b and 9c, evacuation isochron diagrams are compared for the magma recharge versus caldera collapse situation. All relevant geometric and dynamic parameters are identical except for obvious changes in boundary conditions. There are significant differences in the shapes and positions of isochrons for these two cases. Whereas isochrons for the recharge case become tangential at gradually increasing depths, in the caldera collapse case, isochrons continue to migrate laterally. The fact that the size of the quasistagnant region is much smaller in the caldera collapse case implies that zonation effects should be less extreme compared with the recharge case, other factors being identical.

#### APPENDIX A

##### Finite Difference Methods

**Vorticity transport.** Transient solutions to the vorticity transport equation (VTE) were developed using one of two procedures described here. The first method involved an ex-

PLICIT marching procedure (forward time) with space-centered differencing for the diffusion terms and upwind differencing for the advection terms. The formula utilized for the inertial terms is based on the convective form of the vorticity transport equation and may be written

$$\begin{aligned} & \frac{\omega_{ij}^{n+1} - \omega_{ij}^n}{\Delta t} \\ &= -u_{ij} \left( \frac{A_1 \omega_{i+1,j}^n + A_2 \omega_{i,j}^n + A_3 \omega_{i-1,j}^n}{\Delta x} \right) \\ & \quad - v_{ij} \left( \frac{A_4 \omega_{i,j+1}^n + A_5 \omega_{i,j}^n + A_6 \omega_{i,j-1}^n}{\Delta y} \right) \\ & \quad + \frac{1}{Re} (\omega_{i+1,j}^n + \omega_{i-1,j}^n - 2\omega_{ij}^n) / (\Delta x)^2 \\ & \quad + \frac{1}{Re} (\omega_{i,j+1}^n + \omega_{i,j-1}^n - 2\omega_{ij}^n) / (\Delta y)^2 \end{aligned} \quad (A1)$$

In (A1) we have

$$\begin{aligned} A_1 &= +1 & A_2 &= -1 & A_3 &= 0 & u_{ij} &\leq 0 \\ A_1 &= 0 & A_2 &= +1 & A_3 &= -1 & u_{ij} &> 0 \\ A_4 &= +1 & A_5 &= -1 & A_6 &= 0 & v_{ij} &\leq 0 \\ A_4 &= 0 & A_5 &= +1 & A_6 &= -1 & v_{ij} &> 0 \end{aligned}$$

In an effort to find a more efficient and faster VTE solver, a second upwind differencing technique based on the donor cell method of Gentry *et al.* [1966] was used. Average interface velocities on each side of the mesh point are defined and the signs of these velocities determine which value of  $\omega$  is utilized. Note that unlike the first upwind method, this one is conservative. Formally, this method is more accurate than the first since second-order accuracy of the advection terms is retained as in all centered difference schemes. The appropriate equations are

$$\begin{aligned} \frac{\omega_{ij}^{n+1} - \omega_{ij}^n}{\Delta t} &= - \frac{u_R \omega_R - u_L \omega_L}{\Delta x} - \frac{v_T \omega_T - v_B \omega_B}{\Delta y} \\ & \quad + \text{diffusion terms} \end{aligned} \quad (A2)$$

where

$$u_R = \frac{1}{2}(u_{i+1,j}^n + u_{ij}^n) \quad (A3a)$$

$$u_L = \frac{1}{2}(u_{ij}^n + u_{i-1,j}^n) \quad (A3b)$$

$$v_T = \frac{1}{2}(v_{i,j+1}^n + v_{ij}^n) \quad (A3c)$$

$$v_B = \frac{1}{2}(v_{ij}^n + v_{i,j-1}^n) \quad (A3d)$$

and

$$\begin{aligned} \omega_R &= \omega_{ij}^n & u_R &> 0 \\ &= \omega_{i+1,j}^n & u_R &\leq 0 \end{aligned} \quad (A4a)$$

$$\begin{aligned} \omega_L &= \omega_{i-1,j}^n & u_L &> 0 \\ &= \omega_{ij}^n & u_L &\leq 0 \end{aligned} \quad (A4b)$$

$$\begin{aligned} \omega_T &= \omega_{ij}^n & v_T &> 0 \\ &= \omega_{i,j+1}^n & v_T &\leq 0 \end{aligned} \quad (A4c)$$

$$\begin{aligned} \omega_B &= \omega_{i,j-1}^n & v_B &> 0 \\ &= \omega_{ij}^n & v_B &\leq 0 \end{aligned} \quad (A4d)$$

Comparison between the two methods shows that the con-

servative form of the VTE leads to slightly more accurate solutions, although in no case was the difference in vorticity values greater than a few percent. This is consistent with the observations of *Torrance* [1968], who found a similar comparison for a thermally driven cavity flow problem.

Numerical stability conditions are met in practice by specifying the time step according to a criterion based on a von Neumann stability analysis of the vorticity transport expression [Roache, 1972b]. Convergence is ensured so long as

$$\Delta t \leq \left[ \frac{2}{Re} \left( \frac{1}{\Delta x^2} + \frac{1}{\Delta y^2} \right) + \frac{|u|}{\Delta x} + \frac{|v|}{\Delta y} \right]^{-1} \quad (\text{A5})$$

which is a modified Courant condition. Since  $\max |u| < \max |v| = 1$ , by setting  $|u| = |v| = 1$ , a time step ensuring stability could be determined once the mesh size was specified. It has been noted [Noh and Protter, 1963; Roache, 1972a; Runchal and Wolfshtein, 1969] that unidirectional differencing will generate numerical (artificial) viscosity, which can lead to incorrect results. Fortunately, the magnitude of numerically induced viscosity effects can be monitored during a calculation so that the mesh size may be chosen fine enough to ensure an accurate solution to the VTE. The results presented here are consistent with the conclusions of *Campbell and Mueller* [1968], *Gosman et al.* [1969], *Bozeman and Dalton* [1973], and *Torrance* [1968], all of whom obtained meaningful numerical results by using explicit (forward time) upwind differencing methods.

**Poisson equation.** The Poisson equation was solved by a successive overrelaxation (SOR) technique first suggested by *Richardson* [1910] and subsequently modified by many others [e.g., *Frankel*, 1950; *Allen and Southwell*, 1955; *Young*, 1954]. The overrelaxation parameter, which varied slightly with size and shape of the computational domain, was found by numerical experimentation. Values other than the optimum one, while not having much of an effect on the solution, greatly slowed iterative convergence. For example, for a case 1 simulation with  $\delta = 1.75$ , the first iterative cycle through the Poisson expression produced convergence after 500 steps, whereas with the optimum value of 1.91, convergence is achieved after 120 iterations. Since most of the computational time (about 70%) is spent in solving the Poisson equation, an optimum choice of  $\delta$  is essential to minimize the cost of the calculation. The criterion for convergence of the Poisson equation was for the relative error in  $\psi$  at every point in the mesh to be less than one part in  $10^4$ . The finite difference expression used to iteratively solve the Poisson equation was

$$\psi_{ij}^{k+1} = \psi_{ij}^k + \frac{\delta}{4} [\psi_{i-1,j}^k + \psi_{i+1,j}^{k+1} + \psi_{i,j+1}^k + \psi_{i,j-1}^{k+1} + \Delta x^2 \omega_{ij} - 4\psi_{ij}^k] \quad (\text{A6})$$

where  $k$  is introduced as an iteration index.

**Velocity field.** The finite difference expressions used for calculating velocities are standard ones that maintain second-order accuracy. The velocities  $u_{i,j}$  and  $v_{i,j}$  were found according to

$$u_{i,j} = \frac{\psi_{i,j+1} - \psi_{i,j-1}}{2\Delta y} \quad (\text{A7})$$

and

$$v_{i,j} = \frac{\psi_{i-1,j} - \psi_{i+1,j}}{2\Delta x} \quad (\text{A8})$$

where  $\psi_{ij}$ ,  $\Delta x$ , and  $\Delta y$  represent the stream function at mesh

point  $(i, j)$ , the increment in the  $x$  direction, and the increment in the  $y$  direction, respectively. In all of the computations reported on here, a uniform and equant ( $\Delta x = \Delta y$ ) mesh was utilized.

**Boundary vorticity values.** Along boundaries AF, FE, and AB,  $\omega$  is set by the boundary conditions. Since AF is a plane of symmetry along which  $u$  vanishes identically,  $\omega$  is equal to zero there. Along FE and AB,  $\omega$  is easily determined by using the definition of the vorticity and the velocity boundary condition. Along the no-slip boundaries (ED, DC, and CB), the vorticity is not defined a priori and must be determined as part of the solution. The vorticity is easily defined at a grid point embedded in a no-slip wall if it is noted that  $\psi$  is equal to a constant along a wall and  $\partial\psi/\partial n = 0$  normal to that wall. If  $\psi$  is expressed in a direction normal to a no-slip boundary by a Taylor series expansion (e.g., boundary CB),

$$\psi = \psi_{CB} + \left( \frac{\partial\psi}{\partial y} \right)_{CB} y + \frac{1}{2} \left( \frac{\partial^2\psi}{\partial y^2} \right)_{CB} y^2 + \dots \quad (\text{A9})$$

then since  $(\partial\psi/\partial y) = u_{CB} = 0$ , we may use the definition of the vorticity to show that

$$\omega = \left( \frac{\partial v}{\partial x} - \frac{\partial u}{\partial y} \right)_{CB} = \left( \frac{\partial v}{\partial x} - \frac{\partial^2\psi}{\partial y^2} \right)_{CB} = - \left( \frac{\partial^2\psi}{\partial y^2} \right)_{CB} \quad (\text{A10})$$

since  $v = 0$  along the no-slip wall. Now, using (A6) and (A7), it may be shown that

$$\omega_{i,j} = \frac{-2(\psi_{i-1,j} - \psi_{i,j})}{(\Delta x)^2} \quad (\text{A11})$$

for no-slip walls parallel to the  $y$  direction; a correspondingly symmetric relation can also be found for no-slip walls parallel to the  $x$  direction (e.g., DC). This formulation for  $\omega$  was first used by *Thom* [1933].

In the caldera collapse case, the vorticity along boundary DE is slightly different than (A11) because of the nonzero vertical velocity due to roof collapse. By arguments analogous to those given above, the vorticity along DC is found to be

$$\omega_{DE} = \frac{-2}{\Delta x^2} (\psi_{i_p-1,j} - \psi_{i_p,j} - v_p \Delta x) \quad (\text{A12})$$

where  $i_p$  is the value of the  $x$  grid point index along wall DE.

Finally, it is noted that the vorticity at point D, a sharp convex corner, is singular. Although there is no reason to assume continuity or single valuedness of  $\omega$  at point D, some approximation must be made. This problem has been recently addressed by *Holstein and Paddon* [1982], who recommend the procedure used by *Kawaguti* [1965] to determine  $\omega_D$ . This recommendation has been followed here.

#### Lagrangian Particle Tracker

The evacuation isochron diagrams were calculated by following the motion of several hundred marker particles in Lagrangian coordinates by numerical integration of equations of the form

$$\mathbf{X} = \mathbf{X}_0 + \int \mathbf{U} dt \quad (\text{A13})$$

Velocities along an arbitrarily chosen streamline were calculated using a bicubic spline method to interpolate velocities ( $u$  and  $v$ ) defined at nodal points and setting time increments small enough to preserve accuracy without introducing undesirable numerical effects. This procedure resulted in a set of ordered  $(x, y, t)$  values along each streamline. The entire set of

$(x, y, t)$  values were then sorted on the basis of  $t$  values, and the  $x, y$  coordinates of the isochrons could be simply drawn by a standard plotting algorithm.

#### Computational Algorithm

A simulation was initiated by setting values of all internal field parameters equal to zero or as specified by a boundary condition. The vorticity field at the new time level ( $\omega_{i,j}^{k+1}$ ) could then be calculated for all interior mesh points in an explicit manner. Following this, the Poisson equation was solved by iteration by using the new (previously calculated)  $\omega$  values and by updating the stream function values as soon as they became available (i.e., SOR). Generally, the number of iterative cycles required for convergence of the stream function to one part in  $10^4$  varied from 130 at the initiation of a calculation to 1 when the system was near the steady state. Upon attaining convergence in  $\psi$ , the velocity field ( $u$  and  $v$ ) and the vorticity along all no-slip walls could be determined. This completes the determination of the flow field at any particular time. In order to attain the steady state, one returns to the vorticity transport equation, and the entire iterative-sequential process is repeated. Finally, when the vorticity field changes by less than some small quantity between two successive time steps, the steady state has been reached. When the relative change in vorticity values at all  $(i, j)$  changes by less than one part in  $10^4$ , the computation was halted.

In order to ensure that computed results had significance, the number of mesh points was doubled and the entire calculation repeated. This is an expensive test procedure but nevertheless a necessary one in order to verify the code and check the overall stability and veracity of the computational algorithm. In cases when this test was performed, comparison of field values was good to within several percent, becoming slightly poorer for large Reynolds numbers.

For the caldera collapse case the numerical algorithm was modified slightly to take account of the downward moving roof. After each cycle through the complete computational procedure, the finite difference mesh was slightly readjusted in space so that nodal lines coincided with boundaries ED and DC. Values of field variables ( $\psi, \omega, u, v$ ) at the transformed set of nodal points ( $i, j$ ) were determined using values at  $(i, j)$  and a bicubic spline interpolator and the untransformed set of fixed variables. Heuristically, the stability of the solution could be ensured by adopting a small time increment, so that roof subsidence was a very small fraction (1%) of the spatial increment  $\Delta x$ .

A single simulation (case 1) from initial to final (steady) state for  $Re = 10^3$  required about 15 min of CPU time on the IBM 3081D at the Princeton University Computer Center for a domain that included about 4000 nodal points.

#### APPENDIX B

It is the purpose here to show that  $t_{ss} \sim Re$  in the creeping flow and low- $Re$  regime ( $Re < 10$ ) and that in the inertial to subinertial regime ( $Re > 10^3$ ),  $t_{ss}$  is independent of  $Re$ .

As a one-dimensional analog to the transient magma evacuation problem, consider impulsively started Couette flow in a channel of width  $L$ . Suppose that fluid is bounded by two rigid planes at  $x = 0$  and  $x = L$  and is initially at rest. At  $t = 0$  the lower plate is suddenly brought to the constant velocity  $U$  while the upper plate remains fixed. Introducing the dimensionless variables

$$\bar{u} = \frac{u}{U} \quad \bar{x} = \frac{x}{L} \quad \bar{t} = \frac{tU}{L} \quad (\text{B1})$$

the governing equation may be written

$$\frac{\partial \bar{u}}{\partial \bar{t}} = \frac{1}{Re} \frac{\partial^2 \bar{u}}{\partial \bar{x}^2} \quad (\text{B2})$$

The solution of (B2) is

$$\bar{u}(\bar{x}, \bar{t}) = (1 - \bar{x}) - \frac{2}{\pi} \sum_{n=1}^{\infty} \frac{1}{n} \exp\left(\frac{-n^2 \pi^2 \bar{t}}{Re}\right) \sin n\pi \bar{x} \quad (\text{B3})$$

When the summation term on the right-hand side of (B3) is small, the flow will be in the steady state. Steady flow will be attained when the ratio  $\bar{t}/Re$  exceeds some critical value, that is,  $\bar{t}_{ss}/Re = \text{const}$ . Now, in a separate experiment if a higher  $Re$  is initially imposed,  $t_{ss}$  will necessarily increase so that the ratio  $\bar{t}_{ss}/Re$  is maintained constant. Therefore it is shown that  $t_{ss}$  is directly proportional to the first power of  $Re$ .

In the case where inertia is important, the relevant expression for the  $x$  momentum equation is

$$\frac{\partial u}{\partial t} + u \frac{\partial u}{\partial x} + v \frac{\partial v}{\partial y} = \frac{1}{Re} \left( \frac{\partial^2 u}{\partial x^2} + \frac{\partial^2 u}{\partial y^2} \right) \quad (\text{B4})$$

Heuristically one notes that as  $Re$  becomes large, the right-hand side of (B4) vanishes and so solutions to (B4) as  $Re \rightarrow \infty$  cannot depend upon  $Re$ . Therefore  $t_{ss}$  cannot depend upon  $Re$  in the inertial regime.

*Acknowledgments.* Critical reviews by K. Wohletz and an anonymous reviewer improved the quality of this work. Comments from D. A. Yuen, G. Schubert, and Peter Lipman are also gratefully acknowledged. This research was supported by NSF grants EAR81-21200 and EAR81-15728. Sanjay Pande was instrumental in implementation of the numerical code. Funds allocated by the Computer Center of Princeton University are gratefully acknowledged. Jayne Bialkowski typed the manuscript and drafted some of the figures. Computer graphics are by Lucy Noodles.

#### REFERENCES

- Allen, D. N., and R. V. Southwell, Relaxation methods applied to determine the motion in two dimensions, of a viscous fluid past a fixed cylinder, *Quart. J. Mech. Appl. Math.*, **8**, 129-145, 1955.
- Bacon, C. R., Eruptive history of Mount Mazama and Crater Lake caldera, Cascade Range, U.S.A., *J. Volcanol. Geotherm. Res.*, **18**, 57-115, 1983.
- Blake, S., Eruptions from zoned magma chambers, *J. Geol. Soc. London*, **138**, 281-287, 1981.
- Bozeman, J. D., and C. Dalton, Numerical study of viscous flow in a cavity, *J. Comput. Phys.*, **12**, 348-363, 1973.
- Campbell, D. R., and T. J. Mueller, A numerical and experimental investigation of incompressible laminar ramp-induced separated flow, *UNDAS TN-1068-M1*, Dep. of Aero-Space Eng., Notre Dame Univ., South Bend, Indiana, 1968.
- Carmichael, I. S. E., J. Nicholls, F. J. Spera, B. J. Wood, and S. A. Nelson, High temperature properties of silicate liquids: Applications to the equilibration and ascent of basic magma, *Phil. Trans. R. Soc. London, Ser. A*, **286**, 373-431, 1977.
- Cook, H. E., Ignimbrite flows, plugs, and dikes in the southern part of the Hat Creek Range, Nye County, Nevada, in *Studies in Volcanology, Mem. 116*, edited by R. R. Coates, R. L. Hay, and C. A. Anderson, pp. 107-152, Geological Society of America, Boulder, Colo., 1968.
- Crisp, J., Ash flows and lava flows of the Mogan Formation, Gran Canaria: Trace element trends and intensive variables (abstract), *Eos Trans. AGU*, **64**, 883, 1983.
- Crisp, J., Volcanological, mineralogical and petrological studies of the Mogan Formation, Gran Canaria, Canary Islands, Spain, Ph.D. dissertation, Princeton Univ., Princeton, N.J., 1984.
- Curtis, G. H., The stratigraphy of the ejecta from the 1912 eruption of Mount Katmai and Novarupta, Alaska, in *Studies in Volcanology, Mem. 116*, edited by R. R. Coates, R. L. Hay, and C. A. Anderson, pp. 153-210, Geological Society of America, Boulder, Colo., 1968.
- Delaney, P. T., and D. D. Pollard, Solidification of basaltic magma during flow in a dike, *Am. J. Sci.*, **282**, 856-885, 1982.

- Dennis, S. R. C., and F. T. Smith, Steady flow through a channel with a symmetrical constriction in the form of a step, *Proc. R. Soc. London, Ser. A*, 372, 393-414, 1980.
- Erken, E. B., and F. M. Byers, Ash-flow fissure vent in west-central Nevada, *Geology*, 4, 247-251, 1976.
- Frankel, S. P., Convergence rates of iterative treatments of partial differential equations, *Math Tables Other Aids Comput.*, 4, 65-75, 1950.
- Fromm, J. E., The time dependent flow of an incompressible viscous fluid, *Methods Comput. Phys.*, 3, 1964.
- Fromm, J. E., A method for computing non-steady, incompressible viscous fluids, *Rep. LA-2910*, Los Alamos Sci. Lab., Los Alamos, N. M., 1965.
- Gentry, R. A., R. E. Martin, B. J. Daly, An Eulerian differencing method for unsteady compressible flow problems, *J. Comput. Phys.*, 1, 87-118, 1966.
- Giaquinta, A. R., and T. K. Hung, Slow non-Newtonian flow in a zone of separation, *J. Eng. Mech. Div. Am. Soc. Civil Eng.*, 94(EM6), 1968.
- Gosman, A. D., W. Pun, A. K. Runchal, D. B. Spalding, and M. Wolfshtein, *Heat and Mass Transfer in Recirculating Flows*, Academic, New York, 1969.
- Helgeson, H. C., J. M. Delany, H. W. Nesbitt, and D. K. Bird, Summary and critique of the thermodynamic properties of minerals, *Am. J. Sci.*, 278A, 229 pp., 1978.
- Hildreth, E. W., The magma chamber of the Bishop Tuff: Gradients in temperature, pressure and composition, Ph.D. thesis, Univ. of Calif., Berkeley, 1977.
- Hildreth, E. W., The Bishop Tuff: Evidence for the origin of compositional zonation in silicic magma chambers, *Geol. Soc. Am. Spec. Pap.*, 180, 43-75, 1979.
- Hildreth, E. W., Gradients in silicic magma chambers: Implications for lithospheric magmatism, *J. Geophys. Res.*, 86, 10153-10193, 1981.
- Hildreth, E. W., The compositional zoned eruption of 1912 in the Valley of Ten Thousand Smokes, Katmai National Park, Alaska, *J. Volcanol. Geotherm. Res.*, 18, 1-56, 1983.
- Holstein, H., and D. J. Paddon, A finite difference strategy for re-entrant corner flow, in *Numerical Methods for Fluid Dynamics*, edited by K. W. Morton, and M. J. Baines, pp. 341-358, Academic, New York, 1982.
- Housley, R. M., Modeling lunar eruptions, *Proc. Lunar Planet. Sci. Conf. 9th*, 1473-1484, 1978.
- Kawaguti, M., Numerical solutions of the Navier-Stokes equations for the flow in a channel with a step, *MRC TSR 574*, Math. Res. Center, Madison, Wis., 1965.
- Kieffer, S. W., Fluid dynamics of the May 18 blast at Mount St. Helens, *U.S. Geol. Surv. Prof. Pap.*, 1950, 379-400, 1982.
- Korringa, M. K., and D. C. Noble, Ash-flow eruptions from a linear vent area without caldera collapse, *Geol. Soc. Am. Abstr. Programs*, 2, 108-109, 1970.
- Lipman, P. W., Mineral and chemical variations within an ash-flow sheet from Aso caldera, southwestern Japan, *Contrib. Mineral. Petrol.*, 16, 300-327, 1967.
- Lipman, P. W., The roots of ash flow calderas in western North America: Windows into the tops of granitic batholiths, *J. Geophys. Res.*, this issue.
- McBirney, A. R., Compositional variations of the climactic eruption of Mount Mazama, in *Andesite Conference Guidebook*, Bull. 62, edited by H. M. Dole, pp. 53-56, Oregon Department of Geology and Mineral Industries, Portland, 1968.
- McBirney, A. R., Mixing and unmixing of magmas, *J. Volcanol. Geotherm. Res.*, 7, 357-371, 1980.
- Noh, W. F., and M. H. Protter, Difference methods and the equations of hydrodynamics, *J. Math. Mech.*, 12(2), 149-191, 1963.
- Peyret, R., and T. D. Taylor, *Computational Methods for Fluid Flow*, chap. 6, Springer-Verlag, New York, 1983.
- Richardson, L. F., The approximate arithmetical solution by finite differences of physical problems involving differential equations, with an application to the stresses in a masonry dam, *Trans. R. Soc. London, Ser. A*, 210, 307-357, 1910.
- Ritchey, J. L., Divergent magmas at Crater Lake, Oregon: Products of fractional crystallization and vertical zoning in a shallow, water-undersaturated chamber, *J. Volcanol. Geotherm. Res.*, 7, 373-386, 1980.
- Roache, P. J., *Computational Fluid Dynamics*, Hermosa Publishers, Albuquerque, N. M., 1972a.
- Roache, P. J., On artificial viscosity, *J. Comput. Phys.*, 10(2), 351-366, 1972b.
- Rouse, H., Seven exploratory studies in hydraulics, I, Development of the non-circulatory waterspout, *J. Hydraul. Div. Am. Soc. Civil Eng.*, 82, 1038-3 to 1038-7, 1956.
- Rouse, H., and S. Ince, *History of Hydraulics*, Dover Publications, New York, 1963.
- Runchal, A. K., and M. Wolfshtein, Numerical integration procedure for the steady state Navier-Stokes equations, *J. Mech. Eng. Sci.*, 11(5), 445-453, 1969.
- Ryan, M. P., J. Y. K. Blevins, A. T. Okamura, and R. Y. Koyanagi, Magma reservoir subsidence mechanics: Theoretical summary and application to Kilauea Volcano, Hawaii, *J. Geophys. Res.*, 88(B5), 4147-4181, 1983.
- Santin, S. F., F. R. Hernan, L. F. Falcones, and D. P. Dones, Petrographic study of basaltic materials emitted by Teneguia volcano (La Palma, Canary Islands, October 27-November 19, 1971), *Estudios Geologicos*, vol. Teneguia, Instituto de Investigaciones Geologicas, Lucas Mallada, Madrid, 1974.
- Schmincke, H.-U., Ignimbrite sequence on Gran Canaria, *Bull. Volcanol.*, 33, 1199-1219, 1969.
- Schmincke, H.-U., Mineralogy of the ignimbrite sequence on Gran Canaria, Canary Islands, *Geol. Soc. Am. Abstr. Programs, Cordilleran Sect.*, 231-232, 1972.
- Settle, M., Volcanic eruption clouds and the thermal power output of explosive eruptions, *J. Volcanol. Geotherm. Res.*, 68, 6337-6343, 1978.
- Shames, I. H., *Mechanics of Fluids*, 2nd ed., McGraw-Hill, New York, 1982.
- Shapiro, A. H., *The Dynamics and Thermodynamics of Compressible Fluid Flow*, vol. I, John Wiley, New York, 1953.
- Shaw, H. R., Diffusion of H<sub>2</sub>O in granitic liquids, I, Experimental data; II, Mass transfer in magma chambers, in *Geochemical Transport and Kinetics*, edited by A. W. Hoffman, B. J. Gilletti, H. S. Yoder, and R. A. Yund, pp. 139-170, Carnegie Institute of Washington, Washington, D. C., 1974.
- Shaw, H. R., and D. A. Swanson, Eruption and flow rates of flood basalts, in *Columbia River Basalt Symposium*, 2nd Proc., edited by E. H. Gilmour and D. Stradling, Eastern Washington State Press, Cheney, 1970.
- Simuni, L. M., Numerical solutions of several problems of motion of viscous fluid (in Russian), *Eng. J. Acad. USSR*, 4, 1964.
- Smith, R. L., Zones and zonal variations in welded ash flows, *U.S. Geol. Surv. Prof. Pap.*, 354-F, 149-159, 1960.
- Smith, R. L., Ash-flow magmatism, *Geol. Soc. Am. Spec. Pap.*, 180, 5-28, 1979.
- Smith, R. L., and R. A. Bailey, The Bandelier Tuff: A study of ash-flow eruptive cycles from zoned magma chambers, *Bull. Volcanol.*, 29, 83-104, 1966.
- Smith, R. L., and H. R. Shaw, Volcanic rocks as geologic guides to geothermal exploration and evolution, *Eos Trans. AGU*, 54, 1213, 1973.
- Smith, R. L., and H. R. Shaw, Igneous related geothermal systems, *U.S. Geol. Surv. Circ.*, 726, 58-83, 1975.
- Sparks, R. S. J., L. Wilson, and G. Hulme, Theoretical modeling of the generation, movement and emplacement of pyroclastic flows by column collapse, *J. Geophys. Res.*, 83, 1727-1739, 1978.
- Spera, F. J., Ascent and eruption of alkali basalt: Energetics and dynamics, *Geol. Soc. Am. Abstr. Programs*, 15, 1982.
- Spera, F. J., Irreversible thermodynamics and the eruption of volatile-charged magma, *Geol. Mineral. Assoc. Can. Abstr. Programs*, 8, A63, 1983.
- Spera, F. J., and J. A. Crisp, Eruption volume, periodicity and caldera area: Relationships and inferences on development of compositional zonation in silicic magma chambers, *J. Volcanol. Geotherm. Res.*, 11, 169-187, 1981.
- Thom, A., The flow past circular cylinders at low speeds, *Proc. R. Soc. London, Ser. A*, 141, 651-666, 1933.
- Torrance, K., Comparison of finite-difference computations of natural convection, *J. Res. Nat. Bur. Stand.*, 72B(4), 281-301, 1968.
- Tsuya, H., Geological and petrological studies of volcano Fuji, *Tokyo Imp. Univ. Earth. Res. Inst. Bull.*, 33, 341-383, 1955.
- Turner, J. S., *Buoyancy Effects in Fluids*, Cambridge University Press, New York, 1973.
- Wadge, G., The variation of magma discharge during basaltic eruptions, *J. Volcanol. Geotherm. Res.*, 11, 139-168, 1981.
- Wadge, G., Steady state volcanism: Evidence from eruption histories of polygenetic volcanoes, *J. Geophys. Res.*, 87, 4035-4049, 1982.
- Walker, G. P. L., The Taupo pumice: Product of the most powerful known (ultra plinian) eruption?, *J. Volcanol. Geotherm. Res.*, 8, 69-94, 1980.

- Walker, G. P. L., Volcanological applications of pyroclastic studies in *Tephra Studies*, edited by S. Self and R. Sparks, D. Reidel, Hingham, Mass., 1981.
- Walker, G. P. L., and C. J. N. Wilson, Lateral variations in the Taupo ignimbrite, *J. Volcanol. Geotherm. Res.*, 18, 117–133, 1983.
- Wallis, G. B., *One-Dimensional Two-Phase Flow*, McGraw-Hill, New York, 1969.
- Weissberg, H. L., End correction for slow viscous flow through long tubes, *Phys. Fluids*, 5, 1033–1036, 1962.
- Williams, H., The geology of Crater Lake National Park, Oregon, with a reconnaissance of the Cascade Range southward to Mount Shasta, *Carnegie Inst. Wash. Publ.*, 540, 162 pp., 1942.
- Wilson, L., Explosive volcanic eruptions, III, Plinian eruption columns, *Geophys. J. R. Astron. Soc.*, 45, 543–556, 1976.
- Wilson, L., R. S. J. Sparks, T. C. Huang, and N. D. Watkins, The control of volcanic column heights by eruption energetics and dynamics, *J. Geophys. Res.*, 83, 1829–1836, 1978.
- Wilson, L., R. S. J. Sparks, and G. P. L. Walker, Explosive volcanic eruptions, IV, The control of magma properties and conduit geometry on eruption column behaviour, *Geophys. J. R. Astron. Soc.*, 63, 117–148, 1980.
- Worner, G., and H. U. Schmincke, Mineralogical and chemical zonation of the Laacher See tephra sequence, *J. Petrol.*, in press, 1984.
- Young, D., Iterative methods for solving partial difference equations of elliptic type, *Trans. Am. Math. Soc.*, 76, 92–111, 1954.

---

F. J. Spera, Department of Geological and Geophysical Sciences, Guyot Hall, Princeton University, Princeton, NJ 08544.

(Received August 23, 1983;  
revised February 13, 1984;  
accepted March 28, 1984.)